

| | |
|-------------|---|
| Title | Magnetic field depression at the Earth's surface during energetic neutral atom emission fade-out in the inner magnetosphere |
| Author(s) | Nosé, M.; Ohtani, S.; Brandt, P. C:son; Iyemori, T.; Keika, K.; Lee, D.-Y. |
| Citation | Journal of Geophysical Research (2011), 116 |
| Issue Date | 2011-06 |
| URL | http://hdl.handle.net/2433/143677 |
| Right | ©2011. American Geophysical Union. |
| Type | Journal Article |
| Textversion | author |

Magnetic field depression at the Earth's surface during ENA emission fade-out in the inner magnetosphere

Nosé, M.,¹ S. Ohtani,² P. C:son Brandt,² T. Iyemori,¹ K. Keika,³ and D.-Y. Lee⁴

Abstract.

Using data from the high-energy neutral atom (HENA) imager onboard the IMAGE satellite, we examined the relation between the SYM-H index and the ring current energy during a storm main phase. The energy range of the energetic neutral atom (ENA) flux data used here is 16–120 keV for hydrogen and <180 keV for oxygen. From the data for the period 2000–2002, we selected 24 storm main phase events during which the IMAGE satellite was located at a geomagnetic latitude of $\geq 45^\circ$ and a geocentric distance of $\geq 6 R_E$. According to the Dessler-Parker-Sckopke (DPS) equation, the ring current energy is expected to increase as the SYM-H index decreases. When the ENA energy flux is superimposed as a function of the SYM-H index for all 24 events, their overall correlation is negative; that is, the relation between the ENA energy flux and the SYM-H index is generally consistent with the DPS equation. However, an analysis of individual events showed only 10 events (42%) in which the ENA energy flux was negatively correlated with the SYM-H index (negative correlation events). There were 10 events showing no clear correlation between the ENA energy flux and the SYM-H index (no correlation events), and 4 events which contradicted the DPS equation (positive correlation events). In the superimposed plot, we noted that a smooth curve can be drawn for an upper limit of the data distribution, and data from the no correlation or positive correlation events create downward branches in the distribution. These observational results are not explained by the conventional DPS equation but by the “generalized” DPS equation, which includes a term representing energy stored in the stretched magnetic field. We can reasonably presume that the stretched magnetic field prevents energetic particles from being injected into the ring current. From the generalized DPS equation, we conclude that the total (kinetic and magnetic) energy stored in the stretched field and ring current loss mechanisms are important for understanding the relation between the ground magnetic field variation and ring current energy variation.

1. Introduction

Dessler and Parker [1959] derived a simple equation that relates changes in the magnetic field at the center of the Earth (ΔB_C) to the total energy of the ring current (U_K) for three different types of pitch angle distributions: an equatorially mirroring distribution, a field-aligned distribution, and an isotropic distribution. The equation is expressed as

$$-\mu \Delta B_C = 2U_K, \quad (1)$$

where μ is the Earth's dipole moment. Sckopke [1966] showed that any equatorial pitch angle distribution expressed by $\sin^{\gamma} \alpha$ ($\gamma \geq 0$) can satisfy this equation. Thus, equation 1 is now generally known as the Dessler-Parker-Sckopke (DPS) equation. Because of an effect of induction current flowing in the diamagnetic Earth, the change in the magnetic field at the Earth's surface (ΔB_G) becomes larger than ΔB_C by a factor of ξ (i.e., $\Delta B_G = \xi \Delta B_C$), where ξ was estimated to be ~ 1.35 by Rikitake and Sato [1957] and Anderssen and Seneta [1969], ~ 1.33 by Akasofu and Chapman [1972], and

1.24–1.29 by Langel and Estes [1985]. Thus, equation 1 can be rewritten as

$$-\frac{\mu}{\xi} \Delta B_G = 2U_K. \quad (2)$$

Equation 2 predicts a negative correlation between the ground magnetic field variation and the ring current energy; that is, when the ground magnetic field is decreasing (increasing), the ring current is expected to be developing (decaying). However, it should be noted that in deriving the DPS equation; (1) the Earth's magnetic field is assumed to be dipole and not distorted by the ring current; and (2) U_K is assumed to be the ring current energy integrated over infinite volume [Dessler and Parker, 1959; Sckopke, 1966]. Both assumptions, however, are unrealistic. The ring current will deform the Earth's magnetic field lines, and the ring current energy should be confined to a limited region (e.g., within the magnetosphere). Therefore, in the actual magnetosphere, the relation between the ground magnetic field variation and the ring current energy density might be more complicated than that expected from the DPS equation.

Nevertheless, a number of previous studies have used the DPS equation to estimate ΔB_C from the total ring current energy during magnetic storms and compared the estimated ΔB_C with the observed depression of the ground magnetic field, that is, the Dst index. (Note that because $\Delta B_C = \frac{1}{\xi} \Delta B_G \sim (0.74\text{--}0.80) \Delta B_G$, the DPS equation theoretically predicts that the estimated ΔB_C becomes about 75% of the observed Dst index.) For example, using the energetic ion flux data obtained by the AMPTE/CCE satellite, Hamilton *et al.* [1988] showed that the estimated ΔB_C ranges from 24% to 84% of the observed Dst index. Dremukhina *et al.* [1999] and Greenspan and Hamilton [2000] also similarly compared ΔB_C estimated from the AMPTE/CCE data with the Dst index. Roeder *et al.* [1996] concluded that ΔB_C estimated from the CRRES/MICS

¹Data Analysis Center for Geomagnetism and Space Magnetism, Graduate School of Science, Kyoto University, Kyoto, Japan.

²Applied Physics Laboratory, Johns Hopkins University, Laurel, Maryland, USA.

³Center for Solar-Terrestrial Research, New Jersey Institute of Technology, Newark, New Jersey, USA.

⁴Department of Astronomy and Space Science, Chungbuk National University, Chungbuk, Korea.

data by using the DPS equation accounts for 30-50% of the measured Dst index. From a statistical analysis of energetic ion flux data obtained by the Polar/CAMMICE instrument, *Turner et al.* [2001] showed that the estimated ΔB_C contributes, on average, 48-52% of the Dst depression with a large deviation of 25% among individual events. In the past decade or so, numerical calculation has been used to simulate evolution of the ring current in a dipole field [e.g., *Noël*, 1997; *Ebihara and Ejiri*, 2000; *Kozyra et al.*, 1998a; *Jordanova et al.*, 1998; *Liemohn et al.*, 1999]. In such studies, the DPS equation is also adopted to estimate ΔB_C from the total ring current energy obtained by the numerical calculations. The estimated ΔB_C is compared with the observed Dst index to test the relevance of the ring current simulation.

Therefore, the aim of this study is to investigate this relation statistically by using satellite data and to examine the validity of the DPS equation, which has been widely used as described above. The ring current energy is evaluated from the energetic neutral atom (ENA) flux in the energy range of 16-180 keV measured by the high-energy neutral atom (HENA) imager onboard the Imager for Magnetopause-to-Aurora Global Exploration (IMAGE) satellite. High-energy (a few tens to a few hundreds of keV) neutral atoms are created from ring current ions by charge-exchange interactions; they then travel directly from the ring current region to the IMAGE satellite. This process enables us to obtain a global view of the ring current by ENA imaging. Thus, the IMAGE/HENA data are useful for investigating how the ring current develops during magnetic storms and have been used by previous studies [e.g., *C:son Brandt et al.*, 2002a, 2002b; *Mitchell et al.*, 2003, 2005; *Ohtani et al.*, 2005, 2006]. In the present study, we examined temporal variations in the ENA flux during the main phase of 24 geomagnetic storm events. Results showed that some events follow the DPS equation; in other words, the ENA flux increased during the main phase. However, others (more than half of the 24 events) cannot be explained by the DPS equation. We argue that the latter events were caused by a combined effect of magnetic energy generated by field distortion and ring current decay.

This study is organized as follows. In section 2, we describe the instrumentation and data set used in this study. In section 3, we explain how magnetic storm events were selected. In section 4, two typical storm events are studied. One event follows the DPS equation, whereas the other seems not to. Section 5 provides the results of statistical study of the selected storm events. In section 6, we try to explain the observed features in terms of the generalized DPS equation. The effects of the total (kinetic and magnetic) energy stored in the stretched field and the decay of the ring current are discussed, and a simple model calculation is performed to examine temporal variations in the ring current energy and the magnetic field at the Earth's surface. Section 7 provides the conclusion.

2. Instrumentation and Data Set

2.1. IMAGE/HENA

The IMAGE satellite was launched on 25 March 2000 into a polar orbit with a perigee of 1000 km altitude, an apogee of 8.2 R_E , and an orbital period of 14.2 hours. The apsidal line of the orbit was initially inclined at a latitude of 40°, moved over the pole, and returned to 40° after 2 years. The satellite spins at a rate of ~ 0.5 revolution per minute and its spin vector is antiparallel to the orbital angular momentum vector. Overview of the IMAGE satellite can be found in the work of *Burch* [2000]. The HENA imager on board the IMAGE satellite is designed to detect neutral hydrogen atoms in the energy range of ~ 20 -500 keV [*Mitchell et al.*, 2000]. Its field of view is $\pm 60^\circ$ from the satellite spin plane that is divided into 20 polar sectors for lower-energy hydrogen (< 60 keV) and 40 polar sectors for higher-energy hydrogen (> 60 keV). As the satellite spins, the imager sweeps out 360° in the azimuthal direction, which is divided into 60 azimuthal sectors for lower-energy hydrogen (10-60 keV) and 120 azimuthal sectors for higher-energy hydrogen (60-198 keV). This results in one complete 2-D image

of lower-energy (higher-energy) hydrogen flux covering an area of $120^\circ(\text{polar}) \times 360^\circ(\text{azimuth})$ with a $6^\circ \times 6^\circ$ ($3^\circ \times 3^\circ$) angular resolution every 2 min. The energy band is divided into 6 steps for lower-energy hydrogen and 3 steps for higher-energy hydrogen.

The flight software was modified in August 2001, and after that HENA was able to separate oxygen emissions from hydrogen emissions in multiple energy steps (i.e., 7 steps covering the energy range of 29-264 keV) [*Mitchell et al.*, 2003]. Before August 2001, the HENA imager could measure the oxygen ENA flux but only with a single energy step of < 160 keV. (The lower limit of the energy range is approximately 50 keV.) The temporal and spatial resolution of oxygen ENA data are the same as those of lower-energy hydrogen ENA data (i.e., 2 min and $6^\circ \times 6^\circ$) throughout operation. Because of this flight software modification, the HENA-deduced hydrogen ENA flux after August 2001 became about 70% smaller than that before August 2001 [*Keika et al.*, 2006].

The measured ENA flux is the result of a line-of-sight convolution of trapped magnetospheric ion flux, the geocorona density, and the charge exchange cross section. The geocorona density strongly depends on geocentric radial distance (r) and increases exponentially toward Earth [*Rairden et al.*, 1986; *Østgaard et al.*, 2003]. The charge exchange cross section decreases rapidly for H^+ above several tens of keV, while it is rather constant for O^+ over the ring current energy [*Smith and Bewtra*, 1978]. Thus the ENA flux is dependent not only on the ring current intensity but also on spatial/energy distributions of ions. The ENA flux depends on the pitch angle distribution of ring current ions. When the pitch angle distribution changes, the ENA flux possibly changes even if the ring current energy density stays at a constant value [*C:son Brandt et al.*, 2002a; *Ohtani et al.*, 2005].

Nevertheless, recent numerical simulation studies give grounds to consider the ENA flux as a proxy for the ring current intensity. *Fok et al.* [2003, 2006] and *Jones et al.* [2006] computed the ring current ion distributions using the Comprehensive Ring Current Model or the test particle code, reproduced the ENA images from the computed ion distributions, and compared the images with the IMAGE/HENA images. Both images appeared to be similar with regard to spatial distribution and temporal evolution. There were also attempts to extract the equatorial ion fluxes from the ENA images by inversion techniques [e.g., *Perez et al.*, 2001; *Vallat et al.*, 2004]. The consistency between ion fluxes extracted from the HENA and measured locally by the Cluster satellite was reported by *Vallat et al.* [2004], although the extracted ion fluxes had a substantial scatter and a limited dynamic range resulting from the limitations of the inversion technique.

Therefore, in the following analysis, the ENA flux integrated over the inner magnetospheric region is used as an alternative measure of the ring current intensity.

2.2. SYM-H Index

The SYM-H index is essentially the same as the Dst index except that it has a high time resolution of 1 min and it is derived from the average of geomagnetic field variations measured at six low- and mid-latitude stations [*Iyemori et al.*, 1992]. We used the SYM-H index to measure the longitudinally averaged geomagnetic field variations on the surface of the Earth, which can be considered a proxy for the magnetic field changes at the center of the Earth (i.e., ΔB_C). They are related by $\text{SYM-H} \approx \xi \Delta B_C$.

3. Event Selection

From March 2000 through December 2002, we selected magnetic storms that satisfy the following three selection criteria: (1) the minimum value of the SYM-H index is less than -50 nT; (2) during the main phase of the storm, the IMAGE satellite made observations at a geomagnetic latitude of $\geq 45^\circ$ and a geocentric altitude of $\geq 6 R_E$; and (3) during the time intervals that the IMAGE satellite satisfied the above criterion, the SYM-H index was decreasing by more than 30 nT ($|\Delta \text{SYM-H}| > 30$ nT). Criterion 2

is required because we intended to restrict the satellite position to near high geomagnetic latitude and high altitude, where the HENA imager can detect ENAs generated from the entire ring current and avoid contamination due to solar illumination [Ohtani *et al.*, 2005, 2006; Keika *et al.*, 2006]. Criterion 3 is adopted to make the correlation analysis between the SYM-H index and the ENA flux statistically significant, which will be shown in later section. We found 24 storm main phase events using these selection criteria.

4. Event Study

Of the 24 selected storm main phase events, we will show two typical examples in this section. Event 1, which occurred at 1030–1345 UT on 5 October 2000, showed a negative correlation between the SYM-H index and the ENA flux, as expected from the DPS equation (equation (1)). However, Event 2, which occurred at 0630–1119 UT on 28 October 2001, indicated a clear positive correlation between the SYM-H index and the ENA flux. This positive correlation seems to contradict the DPS equation.

4.1. Event 1 (1030–1345 UT on 5 October 2000)

Figure 1a shows the SYM-H index for 5 October 2000. A two-step magnetic storm was initiated by a sudden commencement at 0327 UT. The SYM-H index reached a local minimum of -185 nT at 0718 UT, followed by a temporary recovery until around 1030–1100 UT and a subsequent decrease. The minimum of the SYM-H index was found to be -187 nT at 1345 UT. The event selection criteria give a time interval of 1030–1345 UT, which is indicated by a horizontal bar in the bottom of Figure 1a.

Figures 1b–1e are the IMAGE/HENA images of hydrogen at energies of 16–60 keV at 4 time intervals of 1100–1102 UT, 1150–1152 UT, 1240–1242 UT, and 1330–1332 UT, respectively. These time intervals correspond to open circles shown in the bottom of Figure 1a. In each image, the dipole magnetic field lines at 0000, 0600, 1200, and 1800 magnetic local time (MLT) are drawn for L values of 4 and 8. We found that the ENA flux in the ring current region was increasing gradually when the SYM-H index was decreasing. This result confirms that the SYM-H index was negatively correlated with the ENA flux, which is considered as an alternative measure of the ring current energy. Thus, the event is consistent with expectation from the DPS equation.

4.2. Event 2 (0630–1119 UT on 28 October 2001)

Figure 2 shows the SYM-H index and the IMAGE/HENA images of 16–60 keV hydrogen for 28 October 2001, in the same format as Figure 1. The SYM-H index showed a sudden commencement at 0320 UT and subsequent development of a magnetic storm until its minimum of -150 nT at 1119 UT. A time interval of 0630–1119 UT was determined by the event selection criteria and is indicated by a horizontal bar in the bottom of Figure 2a.

Figures 2b–2e show the HENA images at 0800–0802 UT, 0900–0902 UT, 1000–1002 UT, and 1100–1102 UT, respectively, which correspond to open circles in Figure 2a. From these figures, we noticed that the SYM-H index was decreasing when the ENA flux was clearly decreasing. This can be interpreted as the ground magnetic field being depressed even though the ring current energy was decreasing, which is inconsistent with the DPS equation.

4.3. Correlation Analysis

4.3.1. Calculation of Normalized ENA Energy Flux (Φ_n)

In order to see the relation between the SYM-H index and the ENA flux in more detail, we performed correlation analysis for the above two events. First, we calculated the ENA energy flux (Φ) integrated over the ring current area in a similar way to Keika *et al.* [2006], using

$$\Phi = \iint \hat{n} \cdot (\hat{u}J) E d\Omega dE, \quad (3)$$

where \hat{n} is the unit vector pointing from the center of the Earth to the IMAGE satellite, \hat{u} is the unit vector in the direction of the ENA flux, J is the ENA flux, E is the ENA energy, and Ω is the

solid angle along the line-of-sight. Since the actual HENA data are discrete in energy and solid angle, equation (3) can be rewritten by using summation:

$$\Phi = \sum_i \sum_j \hat{n} \cdot (\hat{u}_i J_{ij}) E_j \Delta\Omega_i \Delta E_j, \quad (4)$$

where subscripts i and j represent physical quantities in the i th pixel (polar \times azimuth) and the j th energy step measured by HENA, and E_j (ΔE_j) is the center energy (the energy band width). The summation for Ω is confined to a polar angle of $\pm 36^\circ$ and an azimuthal angle of $\pm 36^\circ$ excluding the near-Earth area (i.e., a polar angle of $\pm 18^\circ$ and an azimuthal angle of $\pm 18^\circ$), that is, the “doughnut-shaped” area outlined in purple in Figures 1b and 2b. This area covers $r \sim 3$ – $6 R_E$ in the equatorial plane. The summation range for E is 16–60 keV for lower-energy hydrogen ENA and 60–120 keV for higher-energy hydrogen ENA. For oxygen ENA, it is <160 keV for data before August 2001 and 52–180 keV for data after August 2001 (see section 2.1). Next, we computed the normalized energy flux (Φ_n) from the energy flux derived above (Φ), as measured at a radial distance of $8 R_E$, by

$$\Phi_n = \left(\frac{r}{8}\right)^2 \Phi, \quad (5)$$

where r is the radial distance of the satellite position in R_E . In this equation, we expect the ENA flux to decrease with radial distance roughly as r^{-2} [Ohtani *et al.*, 2006]. The above procedure is applied to a series of original ENA images that have a time resolution of 2 min. Finally, we obtain time series of the normalized ENA energy flux with a 2-min resolution, which can be considered a proxy for the total energy of the ring current around $L=3$ – 6 , because ENAs are expected to mostly originate from the near-equatorial plane.

4.3.2. Correlation Between SYM-H and Φ_n

We compared the SYM-H index with Φ_n for Events 1 and 2. Since the original time resolution of the SYM-H index is 1 min, SYM-H was averaged over a 2-min time interval corresponding to that of the HENA measurement. Figures 3a and 3b show the variation in SYM-H and Φ_n , respectively, for Event 1. Red, green, and blue lines in Figure 3b represent Φ_n of 16–60 keV hydrogen, 60–120 keV hydrogen, and <160 keV oxygen. (Here and thereafter, Φ_n is displayed separately in the different species and energy ranges rather than in a combined total flux. This is because the charge exchange cross section strongly depends on the ion species and energy ranges, as stated in section 2.1.) These figures show that Φ_n is negatively correlated with the SYM-H index for all 3 ENA types. Figure 3c gives the result of correlation analysis of these data. The colors of the data points have the same meaning as in Figure 3b. The correlation coefficients were found to be -0.974, -0.972, and -0.694 for 16–60 keV hydrogen, 60–120 keV hydrogen, and <160 keV oxygen, respectively, indicating a strong negative correlation. (Throughout the present paper, the correlation coefficient means the Pearson’s correlation coefficient between SYM-H and Φ_n .) These results are consistent with the prediction of the DPS equation.

In Figures 3d–3f, the SYM-H index and Φ_n for Event 2 are displayed in the same format as in Figures 3a–3c. We can see that both SYM-H and Φ_n show similar variation (Figures 3d and 3e). Correlation coefficients of 0.765, 0.897, and 0.952 were derived for 16–60 keV hydrogen, 60–120 keV hydrogen, and 52–180 keV oxygen, respectively (Figure 3f). These results disagree with the DPS equation.

In Appendix A, we tried to deduce the total energy density from Φ_n of 3 ENA channels for Events 1 and 2. We also found a good negative/positive correlation between SYM-H and the deduced total energy range.

5. Statistical Study

5.1. Classification of Storm Events

For the 24 selected storm events, we calculated correlation coefficients between the SYM-H index and Φ_n for 3 ENA types (i.e.,

low-energy H, high-energy H, and O). Then the events were classified into 3 categories: negative correlation (NC), positive correlation (PC), and no correlation (NoC). The NC category includes storm events in which correlation coefficients are negatively larger than -0.40 for at least two ENA types. The PC category includes storm events showing correlation coefficients larger than 0.40 for at least two ENA types. Storm events that do not fit either the PC or the NC categories are classified into the NoC category. For example, Event 1 is in the NC category and Event 2 is in the PC category. The classification results are summarized in Table 1. It was found that only 42% (=10/24) of the events are classified into the NC category, which is consistent with the DPS equation. In other words, more than half of the events (i.e., 14 events in the PC and NoC categories) cannot be explained by the DPS equation. (One may be interested to see how the classification results shown in Table 1 change if the event selection criterion of $|\Delta\text{SYM-H}|$ is changed. Results in the cases of $|\Delta\text{SYM-H}| > 50$ nT and $|\Delta\text{SYM-H}| > 70$ nT are displayed and discussed in Appendix B.)

Here we briefly give a justification for using 0.40 as a minimum value for declaring a correlation. A linear correlation 0.40 or larger in an absolute value has less than 1% of occurring for uncorrelated parent population if the number of data pairs is larger than 41 [Beverington and Robinson, 1992]. All but 2 of our events include more than 41 data pairs. The number of data pairs of the 2 exceptional events is 23 and 30, and the corresponding probability is less than 6% and 3%, respectively.

5.2. Overall Relation Between SYM-H and Φ_n

We drew a superimposed plot of Φ_n versus SYM-H for all 24 selected events. The results are given in Figure 4. Each panel represents Φ_n of low-energy H, high-energy H, and O for periods before/after August 2001. Colors differentiate the 3 categories: blue for NC, red for PC, and orange for NoC. In all the panels, we can see that overall Φ_n is low when the SYM-H index is close to 0, and Φ_n becomes high when the SYM-H index becomes negatively large. This result is consistent with that of Ohtani et al. [2006]. It may be possible to draw a smooth curve for the upper limit of the data distribution, as indicated by a dotted black line. (No dotted black line is shown in the left panels because the number of events was small.) However, events in the PC and NoC categories (red and orange) have lower Φ_n than events in the NC category (blue), and form downward branches in the distribution. These results suggest that in more than half of the events, the relation between SYM-H and Φ_n deviates from that expected from the DPS equation.

6. Discussion

6.1. Generalized Dessler-Parker-Sckopke Equation

As described in section 1, the DPS equation was originally derived under the assumptions that the Earth's magnetic field is dipole and not distorted by the ring current, and that the ring current energy is integrated over infinite volume [Dessler and Parker, 1959; Sckopke, 1966]. These assumptions have been eliminated by Olbert et al. [1968], Siscoe [1970], and Carovillano and Siscoe [1973], resulting in the generalization of the DPS equation, which includes contributions from the energy in the disturbance magnetic field and from the current flowing on the closed boundary. Iyemori and Rao [1996] and Siscoe and Petschek [1997] interpreted variations in the Dst index at substorm onsets with the generalized DPS equation. Recently, Liemohn [2003] pointed out that in the DPS equation, U_K integrated within a limited volume implicitly includes a contribution from a current flowing on the boundary surface of the limited volume, whereas the contribution appears explicitly in the generalized DPS equation. Vasyliūnas [2006] thoroughly discussed the generalized DPS equation for a volume bounded by closed inner and outer surfaces, which are respectively taken as the Earth's surface and a combination of the magnetopause and a plane perpendicular to the Sun-Earth line at $X = -10 R_E$. Following Siscoe and Petschek [1997], we here chose the boundary to be the magnetopause which is closed by a Y-Z plane located far enough down the tail where currents flowing on/beyond the plane generate negligible magnetic field variations at the center of the Earth. With this

choice of boundary, the generalized DPS equation can be expressed as

$$-\mu\Delta B_C = 2U_K + U_M - U_B, \quad (6)$$

where U_M is the total energy content in the disturbance magnetic field. U_B expresses the contribution from the boundary current (i.e., the magnetopause current or the Chapman-Ferraro current). Now, U_K reflects the total kinetic energy of plasma within the boundary, which can be considered as a sum of the kinetic energies from the ring current, and other regions (or other currents). Although it is difficult to differentiate the ring current from other currents, we suppose that the ring current energy (U_{KR}) is evaluated by the ENA flux measured by IMAGE/HENA. This means that U_{KR} represents the kinetic energy of plasma in the energy range of 16-180 keV and around $L=3-6$. The residual kinetic energy within the boundary is stated as the energy from the near-Earth tail current (U_{KT}), because we can expect that most of the residual energy is contributed by the near-Earth region at $L > 6$ on the nightside. Thus, we obtain $U_K = U_{KR} + U_{KT}$, by which equation 6 can be reformed as follows:

$$\begin{aligned} -\mu\Delta B_C &= 2(U_{KR} + U_{KT}) + U_M - U_B \\ &= 2U_{KR} + (2U_{KT} + U_M) - U_B \\ &= 2U_{KR} + U_S - U_B. \end{aligned} \quad (7)$$

We rewrote $2U_{KT} + U_M$ as U_S , where the subscript "S" represents "stretched", because both U_{KT} and U_M are considered to be related to the stretched magnetic field. (When the tail current energy is large, the tail magnetic field is stretched and a large amount of the magnetic energy is held, and vice versa.) We call U_S the total (kinetic and magnetic) energy stored in the stretched tail magnetic field.

In the next subsections, we test whether the U_S and U_B terms in the generalized DPS equation (equation (7)) are responsible for the observed signatures between the SYM-H index and the ENA flux, in particular, for the 14 events in the PC and NoC categories (Table 1).

6.2. Contribution from U_B

First, we examine whether the contribution from U_B is essential to creating the observed signatures. If so, the events in the PC and NoC categories are expected to disappear by removing the contribution from U_B . Many previous studies found that U_B is correlated with the square root of the solar wind dynamic pressure ($P_{sw} = \rho_{sw} V_{sw}^2$, where ρ_{sw} is the solar wind density and V_{sw} is the solar wind velocity) and wrote it in the following form:

$$U_B = \mu(b\sqrt{P_{sw}} - c), \quad (8)$$

with $b=9-17$ (nT/(nPa) $^{1/2}$) and $c=15-22$ (nT) [Siscoe et al., 1968; Ogilvie et al., 1968; Verzariu et al., 1972; Su and Konradi, 1975; Burton et al., 1975; Gonzalez et al., 1994; Iyemori and Rao, 1997; Kamide et al., 1998]. We adopted $b=13$ (nT/(nPa) $^{1/2}$) and $c=18.5$ (nT), which are intermediate values reported by the previous studies. For the 24 selected events, P_{sw} was calculated from the 1-min resolution data for the solar wind at the Earth's bow shock nose, which are provided on the OMNIWEB page (http://omniweb.gsfc.nasa.gov/ow_min.html). Then we corrected the SYM-H index by removing the contribution from U_B as follows:

$$\text{SYM-H}_C = \text{SYM-H} - \frac{\xi}{\mu} U_B = \text{SYM-H} - \xi(b\sqrt{P_{sw}} - c), \quad (9)$$

where SYM-H_C represents the magnetopause-current-corrected SYM-H index. In the above correction, $\xi=1.3$ was used. As in Table 1 and Figure 4, we classified the events according to the correlation coefficients between SYM-H_C and Φ_n , and drew a superimposed plot of Φ_n versus SYM-H_C . We found that two of the

24 events have a decrease in the SYM- H_C index less than 30 nT; thus, these 2 events were omitted from the statistics. The results are shown in Table 2 and Figure 5. We still found from Table 2 that more than half of the events ($\sim 59\%$ ($=13/22$)) are classified into the PC and NoC categories. Also, Figure 5 shows the same characteristics as Figure 4; that is, (1) it appears that a smooth curve can be drawn for an upper limit of the data distribution, (2) events in the PC and NoC categories (red and orange) have lower Φ_n than events in the NC category (blue), and (3) they form downward branches in the distribution. These results indicate that U_B in the generalized DPS equation does not play a crucial role in the creation of events in the PC and NoC categories.

6.3. Contribution from U_S : Conjecture

The discussion in section 6.2 leads us to consider that the U_S term in the generalized DPS equation is essential to explaining the observational results. When ΔB_C (or ΔB_G) is decreasing, the DPS equation predicts only an increase in U_K (i.e., ring current development), but the generalized DPS equation gives a possibility that U_{KR} can remain constant or decrease (i.e., a stable ring current or ring current decay, as seen by IMAGE/HENA), if U_S is increasing. We presume that this possibility may happen on the basis of the following argument.

The increase in U_S means that the geomagnetic field is stretched and the configuration changes from dipolelike to taillike. Such a stretched geomagnetic field influences the motions of energetic particles in the magnetosphere. Under the guiding center approximation, particle motion can be described by the curvature drift ($\mathbf{W}_C = \frac{2w_{\parallel}}{qB^2}(\mathbf{B} \times (\mathbf{B} \cdot \nabla)\mathbf{B})$), the gradient drift ($\mathbf{W}_{\nabla B} = \frac{w_{\perp}}{qB^3}(\mathbf{B} \times \nabla B)$), and the $\mathbf{E} \times \mathbf{B}$ drift ($\mathbf{W}_{E \times B} = \frac{\mathbf{E} \times \mathbf{B}}{B^2}$), where w_{\parallel} and w_{\perp} are the kinetic energies of particles parallel and perpendicular to the local magnetic field, q is the charge of particles, \mathbf{E} is the electric field vector, and \mathbf{B} is the magnetic field vector. Thus, we obtain $|\mathbf{W}_C| \propto B^{-1} \cdot \rho_C^{-1}$, $|\mathbf{W}_{\nabla B}| \propto \left(\frac{dB}{dx}\right) \cdot B^{-1}$, and $|\mathbf{W}_{E \times B}| \propto E \cdot B^{-1}$, where ρ_C is the curvature radius of the magnetic field lines. We calculated how B , ρ_C , and $\left|\frac{dB}{dx}\right|$ change along the X axis in the nightside magnetosphere for a dipole magnetic field and the modified Tsytanenko 89 model magnetic field (T89c) [Tsytanenko, 1989]. The dipole tile angle was set to 0° for simplicity. The results are shown in Figure 6. A black line and five color lines (from purple to red) denote the dipole field and the T89c model field with $K_p=0-4$, respectively. First, regarding $|\mathbf{W}_C|$, Figures 6a and 6b show that the stretched magnetic field (i.e., the T89c model field with large K_p) generally has a smaller B and a smaller ρ_C than the dipole field in the equatorial plane. Thus, $|\mathbf{W}_C|$ increases in the stretched field. Second, regarding $|\mathbf{W}_{\nabla B}|$, Figure 6c shows that $\left|\frac{dB}{dx}\right|$ decreases in the stretched magnetic field than in the dipole magnetic field. However, its decrease is expected to be overcompensated by B^{-1} , because B shows a more significant decrease than $\left|\frac{dB}{dx}\right|$ (Figure 6a). Furthermore, it includes an additional factor of B^{-1} . Thus, $|\mathbf{W}_{\nabla B}|$ also increases in the stretched magnetic field. Third, we consider $|\mathbf{W}_{E \times B}|$. Recent Geotail observations showed that the duskward convection electric field at $r \sim 9-12 R_E$ is ~ 0.3 mV/m on an average even during the main phase of magnetic storms, which is almost comparable to that during quiet times [Hori et al., 2005, 2006]. It is also well-known that newly injected plasma in the ring current region tends to create the dusk-to-dawn electric field and shield the near-Earth region from the external convective electric field [e.g., Ebihara et al., 2005]. Thus, E can be considered almost constant, but B is decreasing, as seen in Figure 6a; so we can expect that $|\mathbf{W}_{E \times B}|$ also increases in the stretched magnetic field. However, note that $|\mathbf{W}_C|$ and $|\mathbf{W}_{\nabla B}|$ are proportional to the product of two factors that increase in the stretched magnetic field, while $|\mathbf{W}_{E \times B}|$ includes only one such factor. This indicates that $|\mathbf{W}_{E \times B}|$ becomes comparatively smaller than $|\mathbf{W}_C|$ and $|\mathbf{W}_{\nabla B}|$ in the stretched magnetic field. Since \mathbf{W}_C and $\mathbf{W}_{\nabla B}$ point azimuthally westward, and $\mathbf{W}_{E \times B}$ points toward the Earth on the nightside, it becomes more difficult for energetic particles to be injected by convection from the near-Earth plasma

sheet into the ring current in the stretched magnetic field. This will decrease the input rate of U_K , that is, suppress the development of the ring current. Next, we consider that the ring current energy is lost by mechanisms such as charge exchange [e.g., Hamilton et al., 1988; Jordanova et al., 1998; Jorgensen et al., 2001; Kozyra et al., 2002], Coulomb collisions [e.g., Fok et al., 1991, 1993; Jordanova et al., 1996; Ebihara et al., 1998], ion outflow through the dusk-side magnetopause [e.g., Takahashi and Iyemori, 1989; Liemohn et al., 1999; Keika et al., 2005], and ion precipitation into the upper atmosphere [e.g., Kozyra et al., 1998b; Walt and Voss, 2001, 2004].

Therefore, to summarize the argument, if the input rate of U_{KR} decreases in the stretched magnetic field (i.e., increasing U_S) and becomes comparable to or smaller than the loss rate of U_{KR} , the generalized DPS equation gives a constant or decreasing U_{KR} simultaneously with a decreasing ΔB_C (or ΔB_G). The SYM-H index and Φ_n measured by IMAGE/HENA are considered as proxies for ΔB_G and U_{KR} ; thus, it is possible under the generalized DPS equation that Φ_n remains constant or decreases while the SYM-H index is decreasing. In this case, NoC or PC events can be understood. Note that the above argument assumes energy input to U_{KR} only by plasma convection and ignores energy redistribution between U_{KR} and U_S , which may occur during substorms.

6.4. Contribution from U_S : Model

The above conjecture is tested by constructing a simple model. Before magnetic storms, the ring current particle energy ($U_{KR}(t)$ (J)) and the total energy stored in the stretched field ($U_S(t)$ (J)) are set to 0. During the main phase of magnetic storms, we assume that the solar wind has a constant value of the energy input rate (u_0 (Js^{-1})) into the magnetosphere. The solar wind energy is distributed to both $U_{KR}(t)$ and $U_S(t)$ with the energy input rates of $u_{KR}(t)$ (Js^{-1}) and $u_S(t)$ (Js^{-1}), respectively (i.e., $u_0 = u_{KR}(t) + u_S(t)$). Initially, we assume that $u_{KR}(0) = \frac{3}{4}u_0$ and $u_S(0) = \frac{1}{4}u_0$. To include the effect of the stretched magnetic field on the rate of energy input to the ring current, as argued in section 6.3, $u_{KR}(t)$ is taken to depend on $U_S(t)$ by $u_{KR}(t) = u_{KR}(0) \exp(-aU_S(t))$, where a is a positive constant representing the degree of the effect of the stretched magnetic field. $a = 0$ represents no effect of the stretched magnetic field, and a larger a indicates that the stretched magnetic field strongly prevents particles from being injected into the ring current region. The ring current energy loss is assumed to have the form of $\frac{U_{KR}(t)}{\tau}$, where τ is the characteristic time of the energy loss [Burton et al., 1975]. This model is described by the following simultaneous differential equations:

$$\begin{cases} u_0 = u_{KR}(t) + u_S(t), \\ u_{KR}(t) = u_{KR}(0) \exp(-aU_S(t)), \\ \frac{dU_{KR}(t)}{dt} = u_{KR}(t) - \frac{U_{KR}(t)}{\tau}, \\ \frac{dU_S(t)}{dt} = u_S(t). \end{cases} \quad (10)$$

These equations are integrated over time to examine temporal variation in $U_{KR}(t)$ and $U_S(t)$ with $u_0 = 3 \times 10^{11}$ (Js^{-1}), which corresponds to Akasofu's ε parameter, adopting a solar wind speed of 580 km/s and a southward IMF of -18 nT. We selected a and τ from the following sets: $a = (0, 3.0 \times 10^{-16}, 6.0 \times 10^{-16}, 9.0 \times 10^{-16})$ (J^{-1}) and $\tau = (\infty, 10, 5)$ (hr). Integration was made from $t = 0$ (hr) to $t = 8$ (hr). Once $U_{KR}(t)$ and $U_S(t)$ are obtained, we can model $\Delta B_G(t)$ from the equation of $\Delta B_G = -\frac{\xi}{\mu} (2U_{KR} + U_S)$.

The relation between $\Delta B_G(t)$ and $U_{KR}(t)$ is shown in Figure 7 with different values of a and τ . As shown in Figure 7a, if the stretched magnetic field has no effect (i.e., $a = 0$ (J^{-1})), $\Delta B_G(t)$ and $U_{KR}(t)$ are negatively correlated for all values of τ . The blue curves in Figures 7b-7d indicate that even if the stretched magnetic field suppresses particle injection ($a \neq 0$ (J^{-1})), zero energy loss in the ring current ($\tau = \infty$ (hr)) leads to negative correlation or possibly no correlation between $\Delta B_G(t)$ and $U_{KR}(t)$. The yellow and

red curves of Figures 7b-7d indicate that a positive correlation between $\Delta B_G(t)$ and $U_K(t)$ can be realized only by a combination of the effects of the stretched magnetic field and ring current energy loss. In this case, we can see that no correlation is also possible. Furthermore, Figures 7b-7d show that the blue curves give an upper limit for the region where the $\Delta B_G(t)$ - $U_{KR}(t)$ curves run, and that the yellow and red curves form downward branches. These signatures obtained by this model are very similar to those of the IMAGE/HENA results shown in Figures 4 and 5. Thus, we suppose that the conjecture in section 6.3 is plausible, if both the suppression of energy input to the ring current by the stretched magnetic field and the ring current energy loss become effective.

One may consider that the above model is oversimplified and somewhat arbitrary. In an actual solar wind-magnetosphere coupling, u_0 is probably not constant and depends on solar wind conditions. The initial partitioning of the solar wind energy to the ring current and the stretched field may be different from the values used here (i.e., $\frac{3}{4}$ and $\frac{1}{4}$). Second equation of the simultaneous differential equations is solely a postulate, and actual relation between u_{KR} and U_S may be expressed in more complicated form. Although the present simple model reproduced general features between the SYM-H index and Φ_n as shown in Figure 7, more realistic model is needed to ensure the conjecture. A direct test of the conjecture can be performed if the magnetic and electric field measurements become available in multiple locations in the magnetosphere or the near-Earth plasma sheet. This is left for future studies using multiple satellites such as Energization and Radiation in Geospace in Japan and the Radiation Belt Storm Probe in the United States, which plan to measure the magnetic and electric fields along with energetic ion flux in the inner magnetosphere.

6.5. Possible cause for different correlation

In this section, we briefly discuss mechanisms that sufficiently stretch the magnetic field to give rise to NoC and PC events. Figure 8 displays the SYM-H index for all of the 24 storm main phase events in chronological order. Horizontal bar in each panel indicates a time interval determined by the event selection in section 3. Colors mean the 3 different categories, same as Figures 4 and 5: blue for NC, red for PC, and orange for NoC. We notice that 7 NC events (blue) out of 10 occur within a rapid decrease of the SYM-H index within several hours (Exception is event 1, 11 and 24). All of them are preceded by a clear sudden increase of the SYM-H index. These are basic features of magnetic storms generated by interplanetary coronal mass ejections (ICMEs) [e.g., *Tsurutani et al.*, 2006]. On the other hand, almost all of NoC and PC events (orange and red) show gradual decreases of the SYM-H index with a time scale of about 0.5-1 day (Exception is event 22 and 23). They are preceded by no sudden increase or a small increase of the SYM-H index. We find that these events are associated with magnetic storms caused by corotating interaction regions (CIRs) [e.g., *Tsurutani et al.*, 2006] and ICMEs with a weak pressure enhancement. *Turner et al.* [2006] report that geoeffectiveness (the efficiency of energy coupling from the solar wind into the magnetosphere) is larger for CIR-driven storms than for ICME-driven storms, indicating that more power is supplied to the magnetosphere for CIR-driven storms under the same solar wind Poynting flux. We speculate that the differences in the solar wind structure or the geoeffectiveness are related to degree of stretch of the magnetic field, causing the different correlation between SYM-H and Φ_n . More detailed investigation is needed to justify this speculation.

6.6. Issues to be considered

In the previous subsections, we proposed a mechanism to explain the positive correlation between the SYM-H index and the ENA energy flux. However, it is worth briefly stating here that some other effects may contribute to this positive correlation.

6.6.1. Choking of the $E \times B$ transport of plasma

C:son Brandt et al. [2002c] found that the ENA flux at $L \geq 4$ decreased when the IMF B_z kept decreasing at 0800-0909 UT on 4 October 2000, which is similar to our Event 2. They interpreted this

as meaning that the tail magnetic field was stretching rapidly during this time interval, which induced a dusk-to-dawn electric field that opposes the convection electric field. Then the overall electric field is reduced and the $E \times B$ transport of plasma from the tail to the plasma sheet/inner magnetosphere decreases. They called the phenomenon “choking” of the $E \times B$ drift from the tail. Our idea is that the inward $E \times B$ drift increases in the stretched magnetic field, but the azimuthal curvature and gradient drifts increase even more, resulting that it becomes harder for energetic particles to be injected into the ring current. This is similar to the idea of *C:son Brandt et al.* [2002c] in terms that the plasma transport to the inner magnetosphere is “choked,” although a different mechanism weakens the $E \times B$ drift relatively.

6.6.2. Validity of Φ_n as a proxy of the ring current intensity

The evolution of the pitch angle distribution (PAD) of the ring current ions affects Φ_n . As stated in section 2.1, if the PAD was initially isotropic and it gradually changed to become more rounded at $\sim 90^\circ$ (like a pancake distribution) during the main phase, the IMAGE/HENA imager may observe decreases in the ENA intensity from a polar vantage point.

It should be also noted that in calculating Φ_n , we omitted the near-Earth flux, which is generally considered to arise from the interaction between mirroring ions and the dense neutral atmosphere at low altitude. However, as a magnetic storm develops, the location of the ring current shifts Earthward [e.g., *McEntire et al.*, 1985; *Lui*, 1993], causing the origin of the ENA flux created from the ring current ions to shift toward the near-Earth area. Since the ENA flux in the near-Earth area was excluded in calculating Φ_n , this methodology may underestimate Φ_n in case of intense magnetic storms.

7. Summary

We examined the relation between the SYM-H index and the ring current energy during a storm main phase, using data obtained by the IMAGE/HENA imager. The ring current energy was evaluated by the ENA flux at 16-180 keV, which is predominantly generated at $L \sim 3-6$. In Event 1 (1030-1345 UT on 5 October 2000), we found a negative correlation between the SYM-H index and the ENA energy flux, as expected from the DPS equation (equation (1)). However, in Event 2 (0630-1119 UT on 28 October 2001), a clear positive correlation between the SYM-H index and the ENA energy flux was found, which contradicts the DPS equation. We examined the correlation between SYM-H and the ENA energy flux for 24 magnetic storms and classified them into 3 categories: negative correlation (NC), positive correlation (PC), and no correlation (NoC), according to their correlation coefficients. Only 42% ($=10/24$) of the events are in the NC category like Event 1. More than half of the events (i.e., 4 events in the PC category and 10 events in the NoC category) cannot be explained by the DPS equation.

The original derivation of the DPS equation assumed that the Earth's magnetic field is dipole and not distorted by the ring current, and that the ring current energy is integrated over infinite volume [*Dessler and Parker*, 1959; *Sckopke*, 1966]. Since these assumptions are incorrect in the actual magnetosphere, *Olbert et al.* [1968], *Siscoe* [1970], and *Carovillano and Siscoe* [1973] removed them and derived the generalized DPS equation, which includes additional contributions from the energy stored in the stretched magnetic field and from the current flowing on the closed boundary (equations (6) and (7)). The generalized DPS equation can explain the events in the PC and NoC categories, in which the ring current particle energy (U_{KR}) decreases or stays constant, and the total energy stored in the stretched field (U_S) increases. This could happen, because we can reasonably presume that the stretched magnetic field prevents energetic particles from being injected into the ring current; and the ring current energetic particles are lost due to various mechanisms. We described an interaction between U_{KR} and U_S with a simple model and computed numerically the temporal changes in U_{KR} , U_S , and magnetic field disturbances on the ground (ΔB_G). We found that the relation between ΔB_G and U_{KR} is very similar to that obtained from the observations (i.e., the relation between SYM-H and Φ_n), indicating that the above presumption is plausible. Thus, we conclude that the U_S term in the generalized DPS equation, along with ring current loss mechanisms, plays an important role in governing the development and decay of the ring current as well as its relation with ground magnetic field variations.

Appendix A: Deduction of Total Energy Density

With some assumptions, we tried to combine the ENA fluxes of three channels and deduced the total energy density for Events 1 and 2.

The ENA measurement by HENA (J_{ENA}) is a result of the integration through a line-of-sight:

$$J_{\text{ENA}} = \int \sigma \cdot n_{\text{H}} \cdot J_{\text{ION}} \cdot ds, \quad (\text{A1})$$

where σ is the charge exchange cross section, n_{H} is the density of geocorona, J_{ION} is the ring current ion flux, and s is the distance from the HENA imager to the position of ENA production. By assuming that the ring current is flowing only in the equatorial region and has a thickness of Δs , the above equation can be simplified as follows:

$$J_{\text{ENA}} = \sigma_{\text{eq}} \cdot n_{\text{Heq}} \cdot J_{\text{IONeq}} \cdot \Delta s, \quad (\text{A2})$$

where a subscript “eq” means a quantity at the equator. The ENA energy flux (Φ) is given by equation (3) of text. If we assume J_{ENA} is constant over the integration ranges of the energy (E) and the solid angle (Ω), it is simplified as follows:

$$\begin{aligned} \Phi &= J_{\text{ENA}} \cdot E \cdot \Delta E \cdot \Delta \Omega \\ &= \sigma \cdot n_{\text{Heq}} \cdot J_{\text{IONeq}} \cdot \Delta s \cdot E \cdot \Delta E \cdot \Delta \Omega. \end{aligned} \quad (\text{A3})$$

The energy density (ε) of ring current is calculated by

$$\varepsilon = \iiint \frac{1}{2} m v^2 f(v) dv^3, \quad (\text{A4})$$

where m is the ion mass, v is the ion velocity, and f is the velocity distribution function. With help of the equation relating f to J_{ION} , that is, $f = m^2 / (2E) J_{\text{ION}}$, and with an assumption of isotropic ion distribution, we can derive the following equation:

$$\varepsilon = 2\sqrt{2}\pi\sqrt{m} \int \sqrt{E} \cdot J_{\text{ION}} \cdot dE. \quad (\text{A5})$$

Further assumptions that J_{ION} has a finite value only at the equator and is constant over the integration energy range give

$$\varepsilon = 2\sqrt{2}\pi\sqrt{m}\sqrt{E} \cdot J_{\text{IONeq}} \cdot \Delta E. \quad (\text{A6})$$

By substituting J_{IONeq} of equation (A3) into equation (A6), we finally obtain

$$\begin{aligned} \varepsilon &= 2\sqrt{2}\pi\sqrt{m}\sqrt{E} \cdot \frac{\Phi}{\sigma_{\text{eq}} \cdot n_{\text{Heq}} \cdot \Delta s \cdot E \cdot \Delta E \cdot \Delta \Omega} \cdot \Delta E \\ &= \frac{2\sqrt{2}\pi}{n_{\text{Heq}} \cdot \Delta s \cdot \Delta \Omega} \sqrt{\frac{m}{E}} \frac{\Phi}{\sigma_{\text{eq}}} \\ &\propto \sqrt{\frac{m}{E}} \frac{\Phi}{\sigma_{\text{eq}}} \\ &\propto \frac{\Phi}{v \sigma_{\text{eq}}}. \end{aligned} \quad (\text{A7})$$

Therefore, we can deduce the total energy density by summing Φ from the three HENA channels with a weighting factor of $(v \sigma_{\text{eq}})^{-1}$. v can be computed from $v = \sqrt{2\langle E \rangle / m}$, where $\langle E \rangle$ is a typical energy of the channel, that is, $\sqrt{E_{\text{min}} \cdot E_{\text{max}}}$. The charge exchange cross sections for H^+ and O^+ on H are given by Lindsay and Stebbings [2005]. For the 16-60 keV hydrogen, $\langle E \rangle = 31$ keV, $v = 2.44 \times 10^6$ km/s, and $\sigma_{\text{eq}} = 3.14 \times 10^{-16}$ cm². For the 60-120 keV hydrogen, $\langle E \rangle = 85$ keV, $v = 4.04 \times 10^6$ km/s, and $\sigma_{\text{eq}} = 0.212 \times 10^{-16}$ cm². For the 52-160 keV oxygen, $\langle E \rangle = 91$ keV, $v = 1.04 \times 10^6$ km/s, and $\sigma_{\text{eq}} = 3.80 \times 10^{-16}$ cm².

Using these values and equation (A7), we estimated the total energy density for Events 1 and 2. Results of comparison between the

total energy density and SYM-H are shown in Figure A1. The correlation coefficient was found to be -0.935 for Event 1 and 0.899 for Event 2.

Appendix B: Change of Event Selection Criterion

Changing the event selection criterion to be $|\Delta \text{SYM-H}| > 50$ nT and $|\Delta \text{SYM-H}| > 70$ nT, we classified again the events into the NC, PC, and NoC categories. Results are shown in Table B1. This table indicates that even in larger change of SYM-H, we find NoC events. There are still 2 PC events for $|\Delta \text{SYM-H}| > 50$ nT. These results confirm the existence of events that cannot be explained by the DPS equation.

Acknowledgements

We thank D. G. Mitchell and E. C. Roelof for their help in processing the IMAGE/HENA data. Computation of the geomagnetic field using the Tsyganenko model was done with Fortran GEOPACK routines developed by N. A. Tsyganenko and the GSFC modeling group, and IDL GEOPACK DLM provided by H. Korth. This study was supported by Inamori Foundation and the Ministry of Education, Science, Sports and Culture, Grant-in-Aid for Young Scientists (B) (grants 19740303 and 22740322). One of coauthors (P.C.B.) is supported by the National Aeronautics and Space Administration (grant NNX06AC29G) to the Johns Hopkins University Applied Physics Laboratory.

References

- Akasofu, S., and S. Chapman (1972), *Solar-Terrestrial Physics*, 629 pp., Oxford University Press, London.
- Anderssen, R. S., and E. Seneta (1969), New analysis for the geomagnetic Dst field of the magnetic storm on June 18-19, 1936., *J. Geophys. Res.*, 74, 2768–2773, doi:10.1029/JB074i010p02768.
- Beverington, P. R., and D. K. Robinson (1992), *Data reduction and error analysis for the physical sciences*, 2nd ed., McGraw-Hill, Boston.
- Burch, J. L. (2000), IMAGE mission overview, *Space Sci. Rev.*, 91, 1–14.
- Burton, R. K., R. L. McPherron, and C. T. Russell (1975), An empirical relationship between interplanetary conditions and Dst, *J. Geophys. Res.*, 80, 4204–4214, doi:10.1029/JA080i031p04204.
- Carovillano, R. L., and G. L. Siscoe (1973), Energy and momentum theorems in magnetospheric processes., *Reviews of Geophysics and Space Physics*, 11(2), 289–353.
- C:son Brandt, P., D. G. Mitchell, Y. Ebihara, B. R. Sandel, E. C. Roelof, J. L. Burch, and R. Demajistre (2002a), Global IMAGE/HENA observations of the ring current: Examples of rapid response to IMF and ring current-plasmasphere interaction, *J. Geophys. Res.*, 107(A11), 1359, doi:10.1029/2001JA000084.
- C:son Brandt, P., S. Ohtani, D. G. Mitchell, M. Fok, E. C. Roelof, and R. Demajistre (2002b), Global ENA observations of the storm mainphase ring current: Implications for skewed electric fields in the inner magnetosphere, *Geophys. Res. Lett.*, 29(20), 1954, doi: 10.1029/2002GL015160.
- C:son Brandt, P., S. Ohtani, D. G. Mitchell, R. Demajistre, and E. C. Roelof (2002c), ENA observations of a global substorm growthphase dropout in the nightside magnetosphere, *Geophys. Res. Lett.*, 29(20), 1962, doi: 10.1029/2002GL015057.
- Dessler, A. J., and E. N. Parker (1959), Hydromagnetic theory of geomagnetic storms, *J. Geophys. Res.*, 64, 2239–2252, doi: 10.1029/JZ064i012p02239.
- Dremukhina, L. A., Y. I. Feldstein, I. I. Alexeev, V. V. Kalegaev, and M. E. Greenspan (1999), Structure of the magnetospheric magnetic field during magnetic storms, *J. Geophys. Res.*, 104, 28,351–28,360, doi: 10.1029/1999JA900261.
- Ebihara, Y., and M. Ejiri (2000), Simulation study on fundamental properties of the storm-time ring current, *J. Geophys. Res.*, 105, 15,843–15,860, doi:10.1029/1999JA900493.
- Ebihara, Y., M. Ejiri, and H. Miyaoka (1998), Coulomb lifetime of the ring current ions with time varying plasmasphere, *Earth Planets and Space*, 50, 371–382.

- Ebihara, Y., M. Fok, R. A. Wolf, M. F. Thomsen, and T. E. Moore (2005), Nonlinear impact of plasma sheet density on the storm-time ring current, *J. Geophys. Res.*, **110**, A02208, doi:10.1029/2004JA010435.
- Fok, M., J. U. Kozyra, A. F. Nagy, and T. E. Cravens (1991), Lifetime of ring current particles due to Coulomb collisions in the plasmasphere, *J. Geophys. Res.*, **96**, 7861–7867, doi:10.1029/90JA02620.
- Fok, M., J. U. Kozyra, A. F. Nagy, C. E. Rasmussen, and G. V. Khazanov (1993), Decay of equatorial ring current ions and associated aeronomical consequences, *J. Geophys. Res.*, **98**, 19,381–19,393, doi:10.1029/93JA01848.
- Fok, M., et al. (2003), Global ena Image Simulations, *Space Sci. Rev.*, **109**, 77–103, doi:10.1023/B:SPAC.0000007514.56380.f0.
- Fok, M., T. E. Moore, P. C. Brandt, D. C. Delcourt, S. P. Slinker, and J. A. Fedder (2006), Impulsive enhancements of oxygen ions during substorms, *J. Geophys. Res.*, **111**, A10222, doi:10.1029/2006JA011839.
- Gonzalez, W. D., J. A. Joselyn, Y. Kamide, H. W. Kroehl, G. Rostoker, B. T. Tsurutani, and V. M. Vasyliunas (1994), What is a geomagnetic storm?, *J. Geophys. Res.*, **99**, 5771–5792, doi:10.1029/93JA02867.
- Greenspan, M. E., and D. C. Hamilton (2000), A test of the Dessler-Parker-Sckopke relation during magnetic storms, *J. Geophys. Res.*, **105**, 5419–5430, doi:10.1029/1999JA000284.
- Hamilton, D. C., G. Gloeckler, F. M. Ipavich, B. Wilken, and W. Stuedemann (1988), Ring current development during the great geomagnetic storm of February 1986, *J. Geophys. Res.*, **93**, 14,343–14,355, doi:10.1029/JA093iA12p14343.
- Hori, T., et al. (2005), Storm-time convection electric field in the near-Earth plasma sheet, *J. Geophys. Res.*, **110**, A04213, doi:10.1029/2004JA010449.
- Hori, T., et al. (2006), Convection electric field in the near-Earth tail during the super magnetic storm of November 20–21, 2003, *Geophys. Res. Lett.*, **33**, L21107, doi:10.1029/2006GL027024.
- Iyemori, T., and D. R. K. Rao (1996), Decay of the Dst field of geomagnetic disturbance after substorm onset and its implication to storm-substorm relation, *Ann. Geophys.*, **14**, 608–618, doi:10.1007/s005850050325.
- Iyemori, T., and D. R. K. Rao (1997), Reply to the comments by Rostoker et al., *Ann. Geophys.*, **15**, 851–853.
- Iyemori, T., T. Araki, T. Kamei, and M. Takeda (1992), *Mid-latitude geomagnetic indices “ASY” and “SYM” for 1989–1990 (Provisional)*, vol. 1, Data Analysis Center for Geomagnetism and Space Magnetism, Kyoto Univ., Kyoto, Japan.
- Jones, S. T., M. Fok, and P. C. Brandt (2006), Modeling global O⁺ substorm injection using analytic magnetic field model, *J. Geophys. Res.*, **111**, A11S07, doi:10.1029/2006JA011607.
- Jordanova, V. K., L. M. Kistler, J. U. Kozyra, G. V. Khazanov, and A. F. Nagy (1996), Collisional losses of ring current ions, *J. Geophys. Res.*, **101**, 111–126, doi:10.1029/95JA02000.
- Jordanova, V. K., et al. (1998), October 1995 magnetic cloud and accompanying storm activity: Ring current evolution, *J. Geophys. Res.*, **103**, 79–92, doi:10.1029/97JA02367.
- Jorgensen, A. M., M. G. Henderson, E. C. Roelof, G. D. Reeves, and H. E. Spence (2001), Charge exchange contribution to the decay of the ring current, measured by energetic neutral atoms (ENAs), *J. Geophys. Res.*, **106**, 1931–1937, doi:10.1029/2000JA000124.
- Kamide, Y., et al. (1998), Current understanding of magnetic storms: Storm-substorm relationships, *J. Geophys. Res.*, **103**, 17,705–17,728, doi:10.1029/98JA01426.
- Keika, K., M. Nosé, S. Ohtani, K. Takahashi, S. P. Christon, and R. W. McEntire (2005), Outflow of energetic ions from the magnetosphere and its contribution to the decay of the storm time ring current, *J. Geophys. Res.*, **110**, A09210, doi:10.1029/2004JA010970.
- Keika, K., M. Nosé, P. C. Brandt, S. Ohtani, D. G. Mitchell, and E. C. Roelof (2006), Contribution of charge exchange loss to the storm time ring current decay: IMAGE/HENA observations, *J. Geophys. Res.*, **111**, A11S12, doi:10.1029/2006JA011789.
- Kozyra, J. U., V. K. Jordanova, J. E. Borovsky, M. F. Thomsen, D. J. Knipp, D. S. Evans, D. J. McComas, and T. E. Cayton (1998a), Effects of a high-density plasma sheet on ring current development during the November 2–6, 1993, magnetic storm, *J. Geophys. Res.*, **103**, 26,285–26,306, doi:10.1029/98JA01964.
- Kozyra, J. U., M. Fok, E. R. Sanchez, D. S. Evans, D. C. Hamilton, and A. F. Nagy (1998b), The role of precipitation losses in producing the rapid early recovery phase of the Great Magnetic Storm of February 1986, *J. Geophys. Res.*, **103**, 6801–6814, doi:10.1029/97JA03330.
- Kozyra, J. U., M. W. Liemohn, C. R. Clauer, A. J. Ridley, M. F. Thomsen, J. E. Borovsky, J. L. Roeder, V. K. Jordanova, and W. D. Gonzalez (2002), Multistep Dst development and ring current composition changes during the 4–6 June 1991 magnetic storm, *J. Geophys. Res.*, **107**, doi:10.1029/2001JA000023.
- Langel, R. A., and R. H. Estes (1985), Large-scale, near-field magnetic fields from external sources and the corresponding induced internal field, *J. Geophys. Res.*, **90**, 2487–2494, doi:10.1029/JB090iB03p02487.
- Liemohn, M. W. (2003), Yet another caveat to using the Dessler-Parker-Sckopke relation, *J. Geophys. Res.*, **108**(A6), 1251, doi:10.1029/2003JA009839.
- Liemohn, M. W., J. U. Kozyra, V. K. Jordanova, G. V. Khazanov, M. F. Thomsen, and T. E. Cayton (1999), Analysis of early phase ring current recovery mechanisms during geomagnetic storms, *J. Geophys. Res.*, **26**, 2845–2848, doi:10.1029/1999GL900611.
- Lindsay, B. G., and R. F. Stebbings (2005), Charge transfer cross sections for energetic neutral atom data analysis, *J. Geophys. Res.*, **110**, A12213, doi:10.1029/2005JA011298.
- Lui, A. T. Y. (1993), Radial transport of storm time ring current ions, *J. Geophys. Res.*, **98**, 209–214, doi:10.1029/92JA02079.
- McEntire, R. W., A. T. Y. Lui, S. M. Krimigis, and E. P. Keath (1985), AMPTE/CCE energetic particle composition measurements during the September 4, 1984 magnetic storm, *Geophys. Res. Lett.*, **12**, 317–320, doi:10.1029/GL012i005p00317.
- Mitchell, D. G., et al. (2000), High energy neutral atom (HENA) imager for the IMAGE mission, *Space Sci. Rev.*, **91**, 67–112.
- Mitchell, D. G., P. C. Brandt, E. C. Roelof, D. C. Hamilton, K. C. Retterer, and S. Mende (2003), Global imaging of O⁺ from IMAGE/HENA, *Space Sci. Rev.*, **109**, 63–75, doi:10.1023/B:SPAC.0000007513.55076.00.
- Mitchell, D. G., P. C. Brandt, and S. B. Mende (2005), Oxygen in the ring current during major storms, *Adv. Space Res.*, **36**, 1758–1761, doi:10.1016/j.asr.2004.03.025.
- Noël, S. (1997), Decay of the magnetospheric ring current: A Monte Carlo simulation, *J. Geophys. Res.*, **102**, 2301–2308, doi:10.1029/96JA03275.
- Ogilvie, K. W., L. F. Burlaga, and T. D. Wilkerson (1968), Plasma observations on Explorer 34, *J. Geophys. Res.*, **73**, 6809–6824, doi:10.1029/JA073i021p06809.
- Ohtani, S., P. C. Brandt, D. G. Mitchell, H. Singer, M. Nosé, G. D. Reeves, and S. B. Mende (2005), Storm-substorm relationship: Variations of the hydrogen and oxygen energetic neutral atom intensities during storm-time substorms, *J. Geophys. Res.*, **110**, A07219, doi:10.1029/2004JA010954.
- Ohtani, S., P. C. Brandt, H. J. Singer, D. G. Mitchell, and E. C. Roelof (2006), Statistical characteristics of hydrogen and oxygen ENA emission from the storm-time ring current, *J. Geophys. Res.*, **111**, A06209, doi:10.1029/2005JA011201.
- Olbert, S., G. L. Siscoe, and V. M. Vasyliunas (1968), A Simple Derivation of the Dessler-Parker-Sckopke Relation, *J. Geophys. Res.*, **73**, 1115–1116, doi:10.1029/JA073i003p01115.
- Østgaard, N., S. B. Mende, H. U. Frey, G. R. Gladstone, and H. Lauche (2003), Neutral hydrogen density profiles derived from geocoronal imaging, *J. Geophys. Res.*, **108**, 1300, doi:10.1029/2002JA009749.
- Perez, J. D., G. Kozlowski, P. C. Brandt, D. G. Mitchell, J. Jahn, C. J. Pollock, and X. X. Zhang (2001), Initial ion equatorial pitch angle distributions from medium and high energy neutral atom images obtained by IMAGE, *Geophys. Res. Lett.*, **28**, 1155–1158, doi:10.1029/2000GL012636.
- Rairden, R. L., L. A. Frank, and J. D. Craven (1986), Geocoronal imaging with Dynamics Explorer, *J. Geophys. Res.*, **91**, 13,613–13,630, doi:10.1029/JA091iA12p13613.
- Rikitake, T., and S. Sato (1957), The geomagnetic Dst field of the magnetic storm on June 18–19, 1936, *Bull. Earthquake Res. Inst. Tokyo Univ.*, **35**, 7–21.
- Roeder, J. L., J. F. Fennell, M. W. Chen, M. Schulz, M. Grande, and S. Livi (1996), CRRES observations of the composition of the ring-current ion populations, *Adv. Space Res.*, **17**, 17–24, doi:10.1016/0273-1177(95)00689-C.
- Sckopke, N. (1966), A general relation between the energy of trapped particles and the disturbance field near the Earth, *J. Geophys. Res.*, **71**, 3125–3130, doi:10.1029/JZ071i013p03125.
- Siscoe, G. L. (1970), The virial theorem applied to magnetospheric dynamics, *J. Geophys. Res.*, **75**, 5340–5350, doi:10.1029/JA075i028p05340.
- Siscoe, G. L., and H. E. Petschek (1997), On storm weakening during substorm expansion phase, *Ann. Geophys.*, **15**, 211–216, doi:10.1007/s005850050434.
- Siscoe, G. L., V. Formisano, and A. J. Lazarus (1968), Relation between geomagnetic sudden impulses and solar wind pressure changes—An experimental investigation, *J. Geophys. Res.*, **73**, 4869–4874, doi:10.1029/JA073i015p04869.
- Smith, P. H., and N. K. Bewtra (1978), Charge exchange lifetimes for ring current ions, *Space Sci. Rev.*, **22**, 301–318, doi:10.1007/BF00239804.

Figure 1. (a) SYM-H index for 5 October 2000. Horizontal bar represents the time interval of 1030–1345 UT during which IMAGE/HENA data were analyzed. Open circles correspond to times when the IMAGE/HENA images shown in Figures 1b–1e were taken. (b–e) IMAGE/HENA images of hydrogen in an energy range of 16–60 keV at 1100–1102 UT, 1150–1152 UT, 1240–1242 UT, and 1330–1332 UT, respectively. In each image, the dipole magnetic field lines at 0000, 0600, 1200, and 1800 magnetic local time are drawn for L values of 4 and 8. “Doughnut-shaped” area outlined in purple in Figure 1b shows where the ENA energy flux is integrated in section 4.3.1.

Figure 2. (a) Same as Figure 1a, except for the storm main phase on 28 October 2001. Horizontal bar represents the time interval of 0630–1119 UT. (b–e) Same as Figures 1b–1e, except for times of 0800–0802 UT, 0900–0902 UT, 1000–1002 UT, and 1100–1102 UT, respectively.

Figure 3. Variation in (a) the SYM-H index and (b) the normalized ENA energy flux (Φ_n) for 1030–1345 UT on 5 October 2000. Red, green, and blue lines in Figure 3b represent Φ_n of 16–60 keV hydrogen, 60–120 keV hydrogen, and <160 keV oxygen, respectively. (c) Results of correlation analysis for data shown in Figures 3a and 3b. Colors of data points have the same meaning as in Figure 3b. (d–f) Same as Figures 3a–3c, except for the time interval of 0630–1119 UT on 28 October 2001.

Figure 4. Superimposed plot of the normalized ENA energy flux (Φ_n) versus SYM-H for all 24 selected events of the storm main phase. Each panel represents Φ_n for low-energy H, high-energy H, and O before/after August 2001. Color differentiates the 3 categories, that is, blue for NC, red for PC, and orange for NoC. These categories are defined in text. Dotted black lines are possible smooth curves for an upper limit of the data distribution.

Figure 5. Same as Figure 4, except for the magnetopause-current-corrected SYM-H index (the SYM-H_C index).

Figure 6. Variation in B , ρ_C , and $\left|\frac{dB}{dx}\right|$ along the X axis in the nightside magnetosphere for a dipole magnetic field and the modified Tsyganenko 89 model magnetic field (T89c). The dipole tile angle was set to 0° for simplicity. Black line and five color lines (from purple to red) denote the dipole field and the T89c model field with $K_p=0-4$.

- Su, S., and A. Konradi (1975), Magnetic field depression at the earth's surface calculated from the relationship between the size of the magnetosphere and the Dst values, *J. Geophys. Res.*, **80**, 195–199, doi:10.1029/JA080i001p00195.
- Takahashi, S., and T. Iyemori (1989), Three-dimensional tracing of charged particle trajectories in a realistic magnetospheric model, *J. Geophys. Res.*, **94**, 5505–5509, doi:10.1029/JA094iA05p05505.
- Tsurutani, B. T., R. L. McPherron, W. D. Gonzalez, G. Lu, N. Gopalswamy, and F. L. Guarnieri (2006), Magnetic storms caused by corotating solar wind streams, in *Recurrent Magnetic Storms: Corotating Solar Wind Streams*, *Geophys. Monogr. Ser.*, vol. 167, edited by B. T. Tsurutani, R. L. McPherron, W. Gonzalez, G. Lu, J. H. A. Sobral, and N. Gopalswamy, pp. 1–17, AGU, Washington, D.C., doi:10.1029/167GM03.
- Tsyganenko, N. A. (1989), A magnetospheric magnetic field model with a warped tail current sheet, *Planet. Space Sci.*, **37**, 5–20, doi:10.1016/0032-0633(89)90066-4.
- Turner, N. E., D. N. Baker, T. I. Pulkkinen, J. L. Roeder, J. F. Fennell, and V. K. Jordanova (2001), Energy content in the storm time ring current, *J. Geophys. Res.*, **106**, 19,149–19,156, doi:10.1029/2000JA003025.
- Turner, N. E., E. J. Mitchell, D. J. Knipp, and B. A. Emery (2006), Energetics of magnetic storms driven by corotating interaction regions: A study of geoeffectiveness, in *Recurrent Magnetic Storms: Corotating Solar Wind Streams*, *Geophys. Monogr. Ser.*, vol. 167, edited by B. T. Tsurutani, R. L. McPherron, W. Gonzalez, G. Lu, J. H. A. Sobral, and N. Gopalswamy, pp. 113–124, AGU, Washington, D.C., doi:10.1029/167GM11.
- Vallat, C., et al. (2004), First comparisons of local ion measurements in the inner magnetosphere with energetic neutral atom magnetospheric image inversions: Cluster-CIS and IMAGE-HENA observations, *J. Geophys. Res.*, **109**, A04213, doi:10.1029/2003JA010224.
- Vasyliūnas, V. M. (2006), Ionospheric and boundary contributions to the Dessler-Parker-Sckopke formula for Dst, *Ann. Geophys.*, **24**, 1085–1097.
- Verzari, P., M. Sugiura, and I. B. Strong (1972), Geomagnetic field variations caused by changes in the quiet-time solar wind pressure, *Planet. Space Sci.*, **20**, 1909–1914, doi:10.1016/0032-0633(72)90123-7.
- Walt, M., and H. D. Voss (2001), Losses of ring current ions by strong pitch angle scattering, *Geophys. Res. Lett.*, **28**, 3839–3841, doi:10.1029/2001GL013425.
- Walt, M., and H. D. Voss (2004), Proton precipitation during magnetic storms in August through November 1998, *J. Geophys. Res.*, **109**, A02201, doi:10.1029/2003JA010083.

Figure 7. (a) Relation between the ground magnetic field variations ($\Delta B_G(t)$) and the ring current particle energy ($U_{KR}(t)$) computed with the model proposed here. The degree of the effect of the stretched magnetic field (a) and the rate of energy input into the magnetosphere (u_0) were assumed to be $a = 0$ (J^{-1}) and $u_0 = 3 \times 10^{11}$ (Js^{-1}). Blue, orange, and red curves represent the characteristic time of energy loss (τ) of ($\infty, 10, 5$) (hr), respectively. (b-d) Same as Figure 7a, except for different values of $a = (3.0 \times 10^{-16}, 6.0 \times 10^{-16}, 9.0 \times 10^{-16})$ (J^{-1}).

Figure 8. The SYM-H index for all of the 24 storm main phase events in chronological order. Horizontal bar in each panel indicates a time interval determined by the event selection. Colors mean the 3 different categories: blue for NC, red for PC, and orange for NoC.

Figure A1. Results of correlation analysis between the deduced total energy density and SYM-H (top) for Event 1 and (bottom) for Event 2.

Table 1. Classification of 24 selected storm events according to correlation coefficients between the SYM-H index and Φ_n .

| Category | Number of Events |
|---------------------------|------------------|
| Negative Correlation (NC) | 10 |
| Positive Correlation (PC) | 4 |
| No Correlation (NoC) | 10 |

Table 2. Classification of 22 events according to correlation coefficients between the SYM-H_C index and Φ_n .

| Category | Number of Events |
|---------------------------|------------------|
| Negative Correlation (NC) | 9 |
| Positive Correlation (PC) | 4 |
| No Correlation (NoC) | 9 |

Table B1. Reclassification of events when the selection criterion of $|\Delta \text{SYM-H}|$ is changed.

| Category | Number of Events | | |
|---------------------------|---------------------------------|---------------------------------|---------------------------------|
| | $ \Delta \text{SYM-H} > 30$ nT | $ \Delta \text{SYM-H} > 50$ nT | $ \Delta \text{SYM-H} > 70$ nT |
| Negative Correlation (NC) | 10 | 6 | 4 |
| Positive Correlation (PC) | 4 | 2 | 0 |
| No Correlation (NoC) | 10 | 5 | 3 |

Figure 1

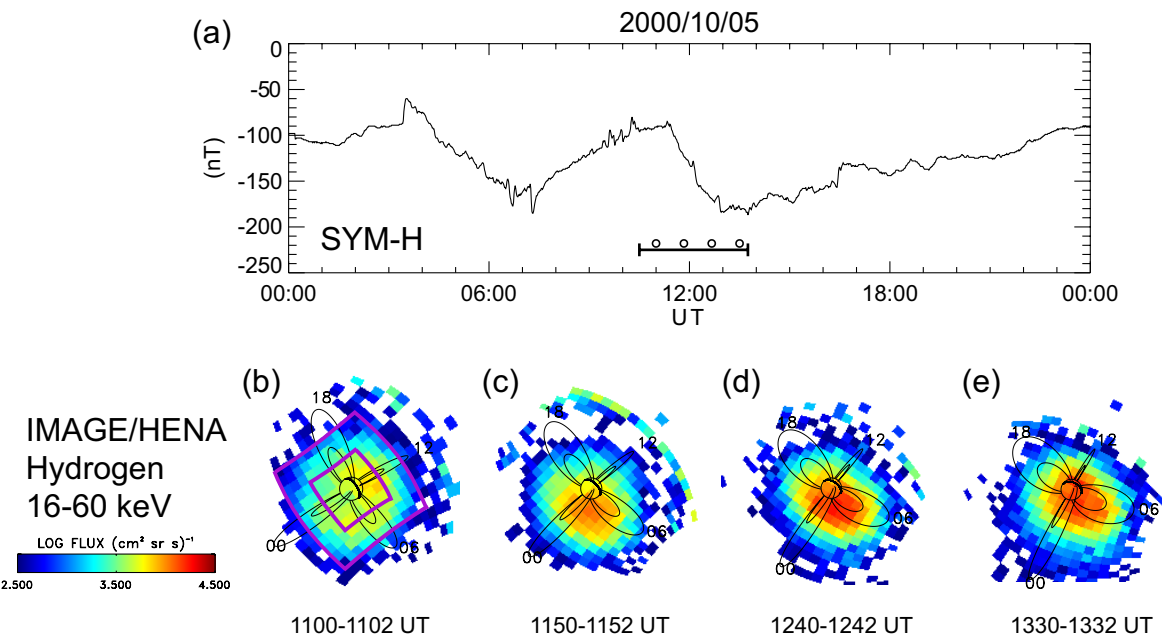


Figure 2

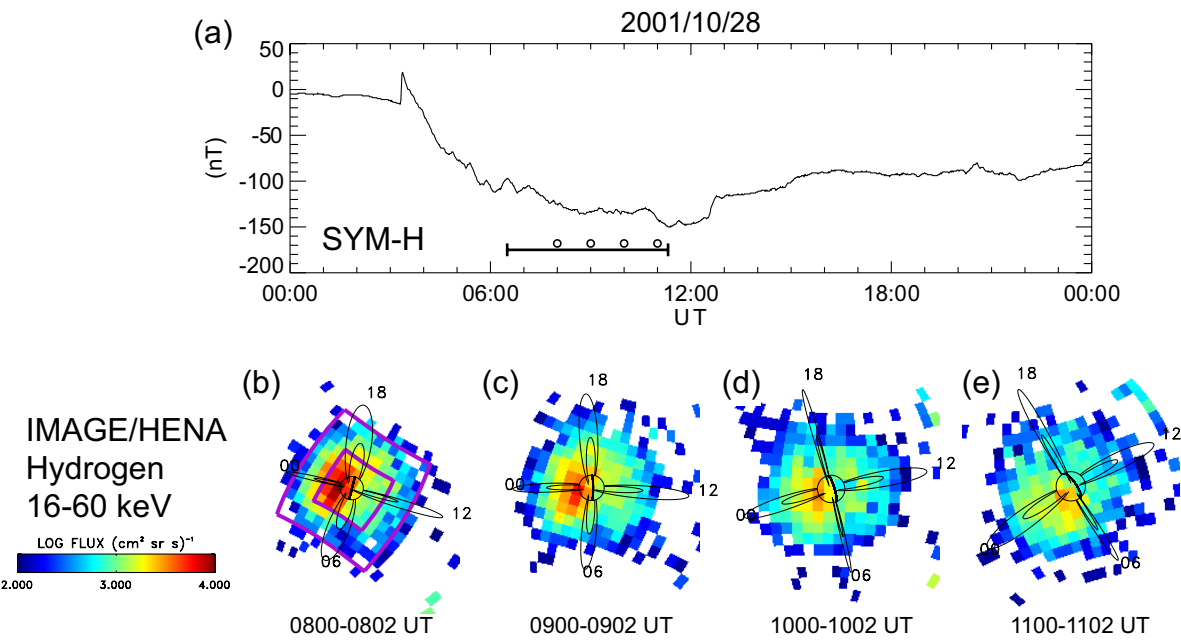


Figure 3

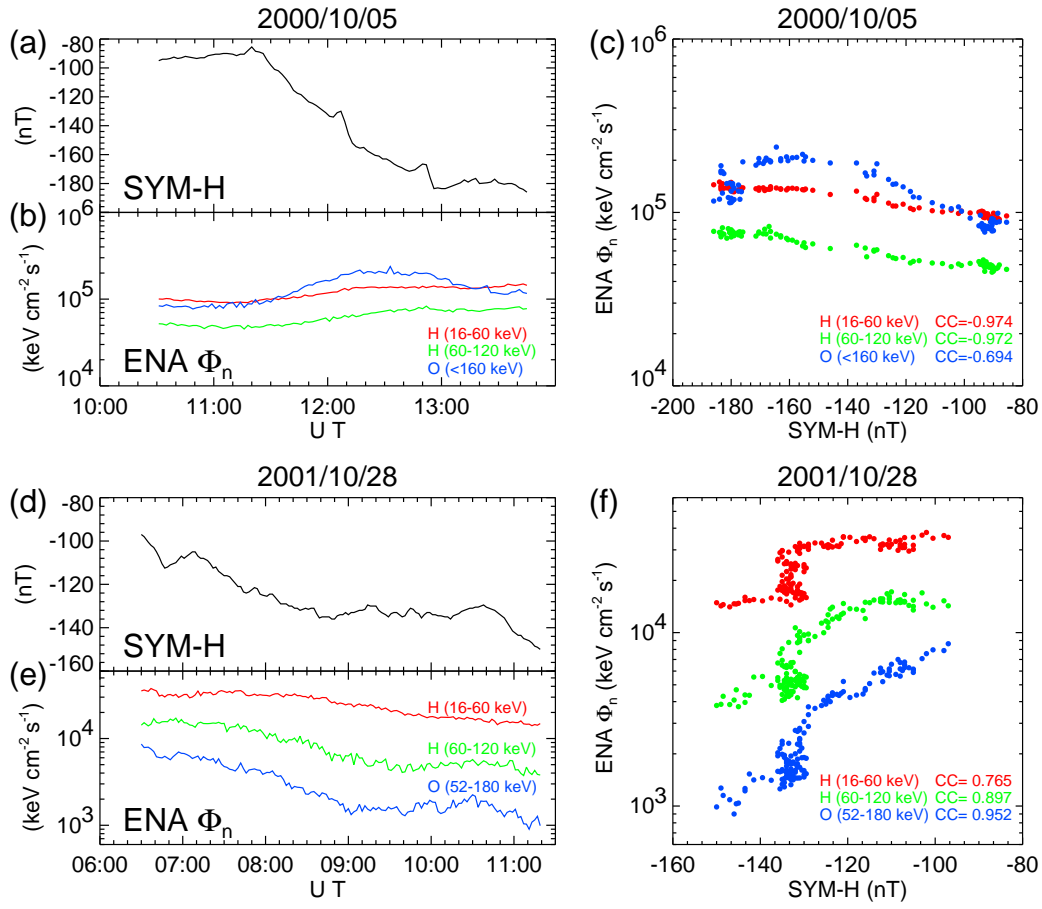


Figure 4

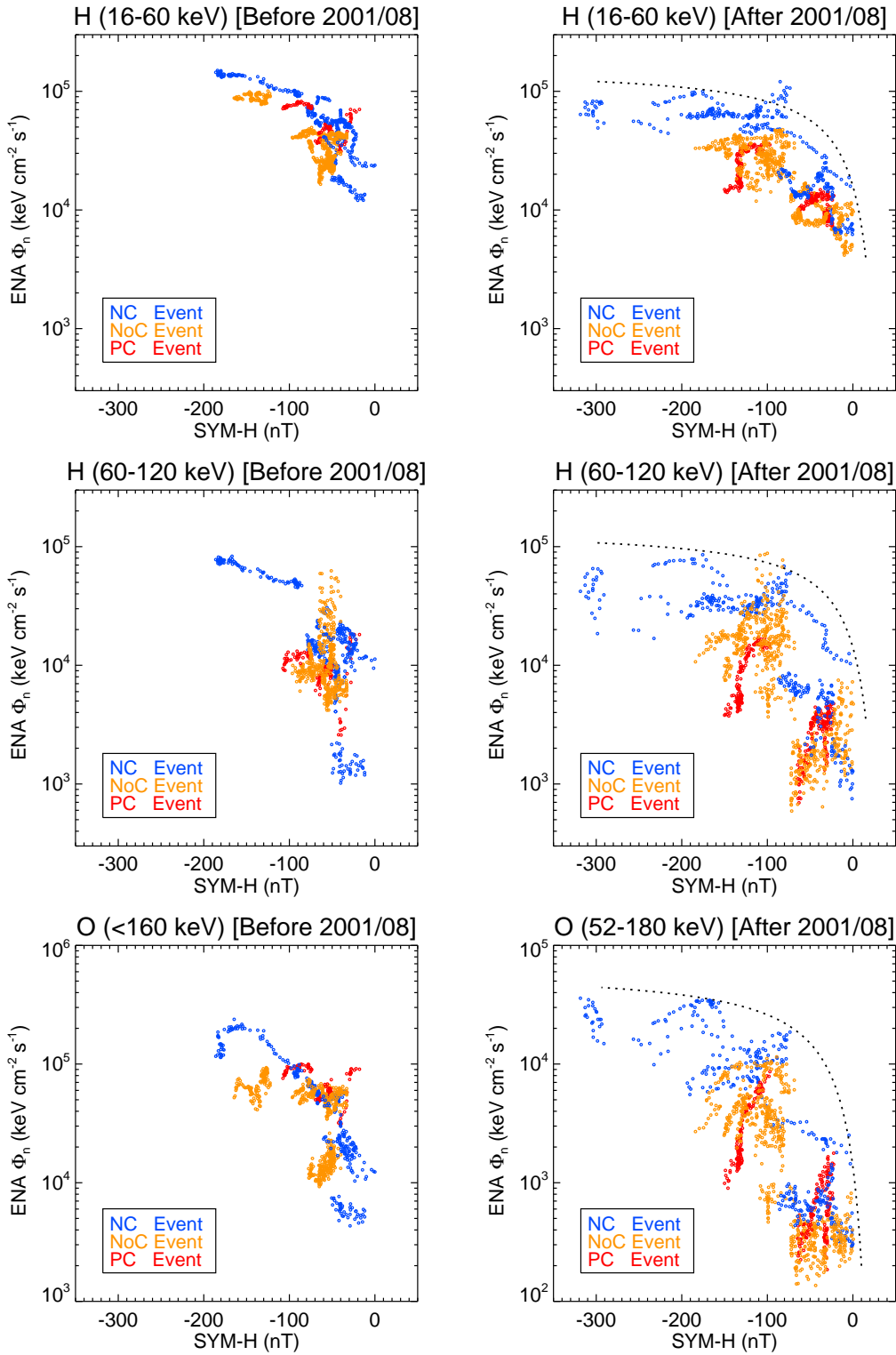


Figure 5

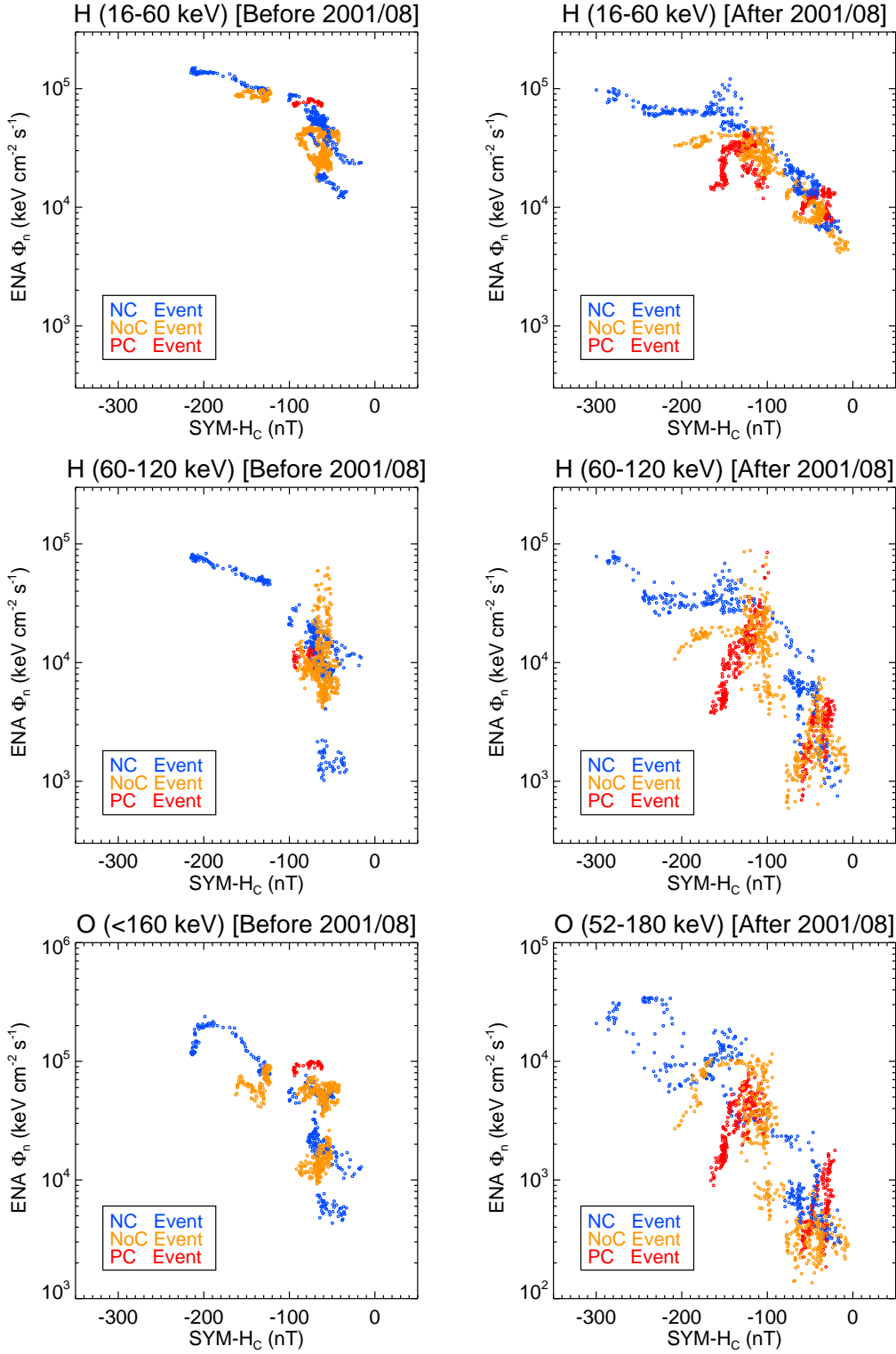


Figure 6

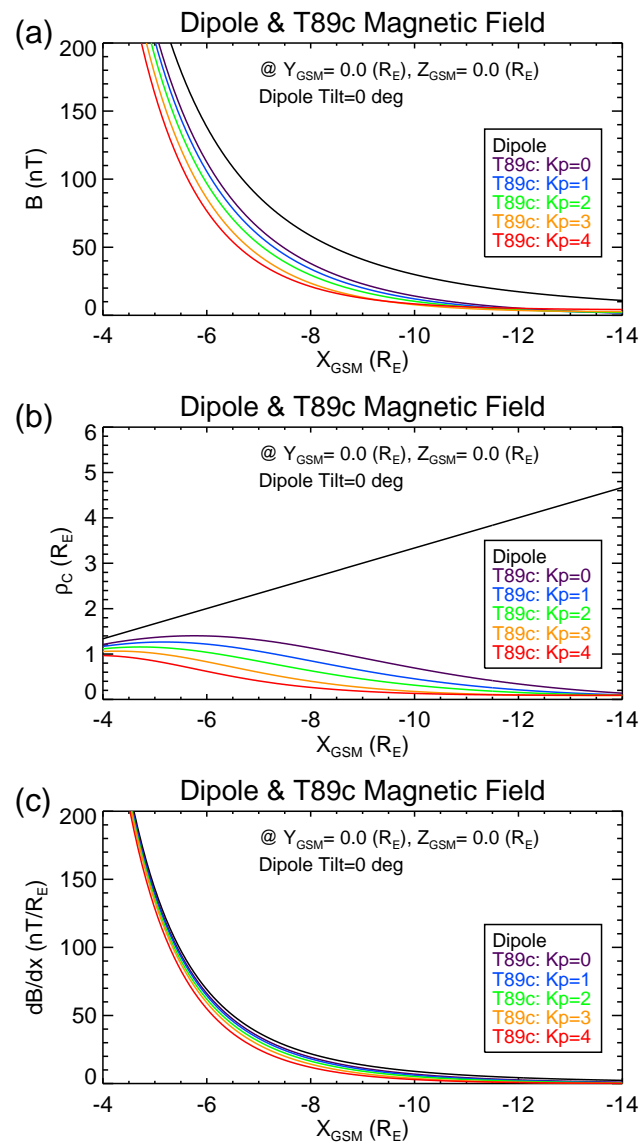


Figure 7

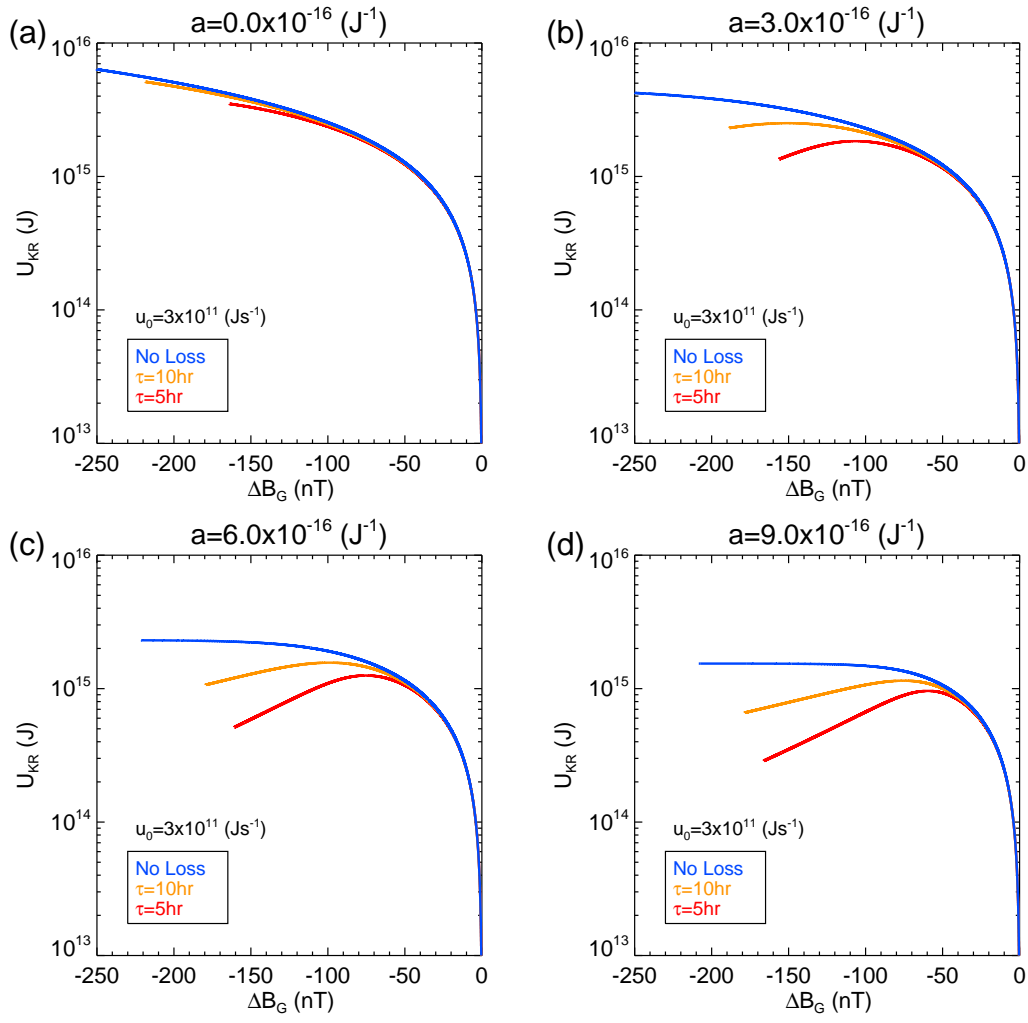


Figure 8

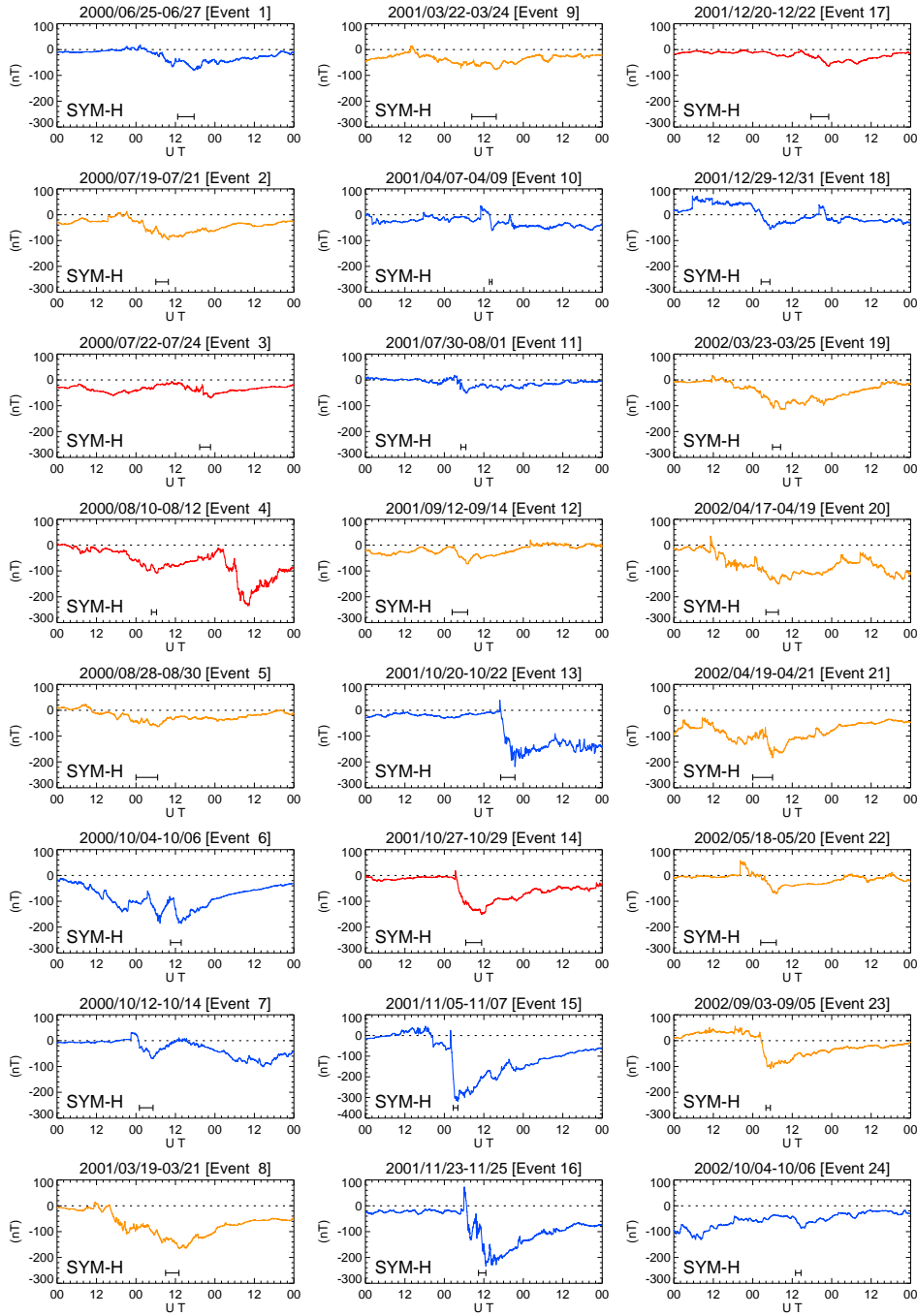


Figure A1

